Chemistry–A European Journal
Research Article
doi.org/10.1002/chem.202200490
Chemistry Europe
European Chemical Societies Publishing
www.chemeurj.org

Influence of the Linker Chemistry on the Photoinduced Charge-Transfer Dynamics of Hetero-dinuclear Photocatalysts

Linda Zedler,[a] Carolin Müller,[b] Pascal Wintergerst,[c] Alexander K. Mengele,[c] Sven Rau,[c] and Benjamin Dietzek-Ivanšić*[a, b]

Abstract: To optimize light-driven catalytic processes, light-mediated multi-electron transfer dynamics in molecular dyads need to be studied and correlated with structural changes focusing on the catalytically active metastable intermediates. Here, spectro-electrochemistry has been employed to investigate the structure-dependent photoelectron transfer kinetics in catalytically active intermediates of two Ru–Rh catalysts for light-driven NAD^+ reduction. The excited-state reactivity of short-lived intermediates was studied along different photoreaction pathways by resonance Raman and time-resolved transient absorption spectro-electrochemistry with sub-picosecond time resolution under *operando* conditions. The results demonstrate, for the first time, how the bridging ligand serves as a (multi-)electron storage structure, mediates the strength of the electronic coupling of catalytic and photocenter and impacts the targeted electron transfer as well as parasitic electron-transfer kinetics.

Introduction

Recently, much attention has been paid to multi-component artificial photocatalytic water reduction systems with covalent linkage between a photosensitizer and a (hydrogen evolving) catalyst.[1] This configuration offers synthetic handles to tune key function-determining reaction steps, for example, light absorption and intramolecular electron transfer, by molecular design.[2] As the overall catalyst's performance largely depends on directional intramolecular electron transfer processes between the photosensitizer and catalyst modules, the bridging ligands (BLs) play a key role in designing the catalysts and evaluating its function and stability. Structural modification of the BL represents a direct path to influence the photophysics and thus also the efficiency of the light-driven catalyst.[3] Ideally, the photostable bridging ligand should i) promote directional electron transfer from the excited state to the catalytic active site and ii) act as an electron reservoir during electron transfer cascades (Scheme 1).[2,4] However, when using the bridging ligand for electron storage, the transfer of further photoelectrons across the bridge might be inhibited and these photoelectrons are then redirected to peripheral ligands.[5] Whether additional charge injection into the terminal ligands instead of the BL benefits[6] or impedes the overall catalytic process,[7] cannot be answered generally yet and is a matter of debate for individual catalyst's structures.

Despite the importance of understanding the light-driven intramolecular charge-transfer processes in molecular dyads and their relation to the light-driven catalytic activity, mechanistic investigations on such systems have focused to a large extend on the charge transfer cascades induced by absorption of a single photon. Hence, the mechanism of subsequent electron transfer steps, yielding the catalytically active species, remain quite generally poorly understood. Accordingly, it is necessary to study ultrafast electron transfer processes in singly (or twofold) reduced intermediates of the light-driven catalytic cycles (Scheme 1). Experimentally such intermediates can be selectively produced and characterized by spectro-electrochemistry. Consequently, time-resolved transient absorption spectro-electrochemistry has been established as a suitable means to study photoinduced (charge-transfer) processes in such reduced intermediates of molecular species in solution[8] or molecularly functionalized metal oxide surfaces.[9] In previous work utilizing ultrafast transient absorption spectro-electrochemistry,[3] we identified light-induced electron transfer from a twofold reduced catalytic Rh(Cp*) center to the molecular bridge as a deactivation pathway in the molecular photocatalyst $[(tbbpy)_2Ru(tpphz)Rh(Cp^*)]^{2+}$ (tbbpy = 4,4′-di-*tert*-butyl-2,2′-bi-

[a] *Dr. L. Zedler, Dr. B. Dietzek-Ivanšić*
Department Functional Interfaces
Leibniz Institute of Photonic Technology Jena (Leibniz-IPHT)
Albert-Einstein-Straße 9, 07745 Jena (Germany)
E-mail: benjamin.dietzek@leibniz-ipht.de

[b] *Dr. C. Müller, Dr. B. Dietzek-Ivanšić*
Institute of Physical Chemistry
Friedrich Schiller University Jena
Helmholtzweg 4, 07743 Jena (Germany)

[c] *P. Wintergerst, Dr. A. K. Mengele, Dr. S. Rau*
Department of Inorganic Chemistry I, Ulm University
Albert-Einstein-Allee 11, 89081 Ulm (Germany)

Supporting information for this article is available on the WWW under https://doi.org/10.1002/chem.202200490

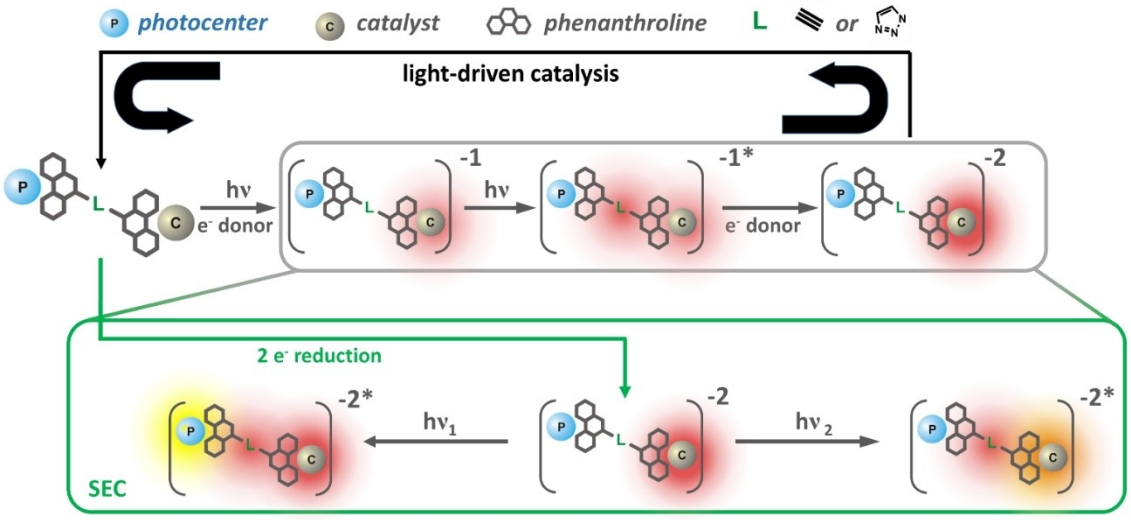

Scheme 1. The catalytic cycle for light-driven catalysis to molecular hydrogen involves the accumulation of two electrons at the catalytic center generated by the subsequent absorption of two photons and the regeneration of the photocenter by an electron donor. The first electron transfer can be analyzed by time-resolved spectroscopy, but further electron transfer steps are not accessible by optical techniques. The combination of spectroscopic techniques with electrochemistry enables the generation of the semistable intermediate of the catalytic cycle. Time-resolved spectroscopy of the intermediate enables the study of the transfer of a third photoelectron across the bridging ligand, competing reaction channels, and the localization of the charges as well as the (photo)stability and lifetime of the intermediate.

pyridine, tpphz = tetrapyridophenazine, Cp* = pentamethylcyclopentadienyl).

This work focusses on two other Ru–Rh dyads, in which the $(NN)_2$Ru photosensitizer (NN = α-diimine ligand) is intramolecularly linked to a Rh(Cp*)Cl catalyst as well. We used time-resolved transient absorption spectro-electrochemistry to evaluate the impact of the molecular bridges on the light-driven multi electron processes and its ability to accumulate and stabilize photoinduced charges – either on the bridging ligand itself or on the catalytically active Rh(Cp*) center, as depicted in Scheme 1 in $[(NN)_2Ru\text{-}BL\text{–}Rh(Cp^*)Cl]^{3+}$.

The two bridging ligands investigated in this work consist of 1,10-phenanthroline (phen) coordination spheres on both, the $(tbbpy)_2$Ru light absorbing unit as well as the Rh(Cp*)Cl catalyst unit and are either bridged via an alkyne (Ru^{II}–≡–Rh^{III}) or a triazole group (Ru^{II}–trz–Rh^{III}, Figure 1A). A triazole linker has previously also been used to construct dinuclear Ru–Re complexes for light-driven CO_2 reduction.[10] The impact of the linkers' structures on the photocatalytic performance towards NADH formation has been recently demonstrated.[11] Ru^{II}–≡–Rh^{III} is a highly efficient photocatalyst for NAD^+ reduction even outpacing conventional thermal catalysis. Its high initial activity roots in a by a factor of 6 more efficient formation of the catalytically competent twofold reduced Rh^I species, thus surpassing the initial rate of NAD^+ reduction of Ru^{II}-trz-Rh^{III} also by a factor of 6. However, Ru^{II}–≡–Rh^{III} suffers rapid deactivation during photocatalysis. This deactivation was associated with alterations of the triple bond during operando conditions.

To this end, the study at hand is to shed light on the electron transfer in the twofold reduced photocatalysts Ru^{II}–≡–Rh^I and Ru^{II}–trz–Rh^I and to investigate the impact of optical excitation of the twofold reduced intermediate on the deactivation of the catalyst under operando conditions.

Results and Discussion

Cyclic voltammograms of Ru^{II}–≡–Rh^{III} and Ru^{II}–trz–Rh^{III} in a custom made spectro-electrochemical cell show up to three reduction waves (Figure 1B inset, Figure S1 in the Supporting Information). The first wave is assigned to a two-electron reduction of the Rh^{III}/Rh^I redox couple accompanied by a loss of a chloride ligand.[12] The second reduction wave causes reduction of the bridging ligand, that is, of the 1,10-phenathroline (phen) fragment in the ruthenium sphere.[3,11,13] At even more negative potential the peripheral tbbpy ligands become reduced.[13a,14]

UV-vis spectro-electrochemistry reveals that upon twofold reduction of Ru^{II}–≡–Rh^{III} and Ru^{II}–trz–Rh^{III}, that is, upon generation of the respective Rh^I complexes, Ru^{II}–≡–Rh^I and Ru^{II}–trz–Rh^I, a new absorption band arises. This band at 700 nm was previously assigned to a Rh^I→phen MLCT transition (Figures 1B and S1), which is supported by TD-DFT (S_6 in Table S3 and S5).[3] Moreover, the absorbance between 400 and 500 nm increases after applying the first and second reduction potential. This is associated with the rise of additional π–π* absorption features of the reduced phen sphere (at *ca.* 480 nm).[15] According to the TD-DFT predictions, these π–π* are mixed with Rh^I→phen (Rh-MLCT) absorption features (see S_{19} in Table S3 and S_{15} in Table S5). The absorption band at 345 nm, which stems from π–π* transitions delocalized across the –≡– bridge of Ru^{II}–≡–Rh^{III},[11,16] loses intensity during the second reduction wave (Figure 1B).

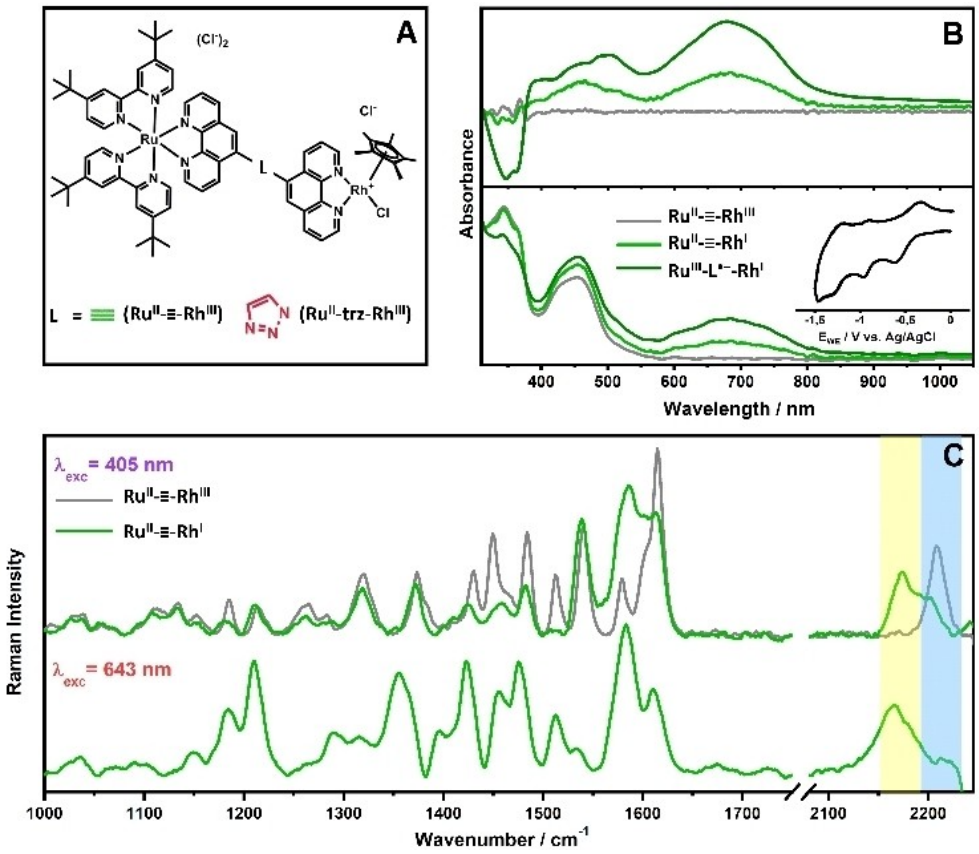

Figure 1. A) Structure of catalysts Ru^{II}–≡–Rh^{III} and Ru^{II}–trz–Rh^{III}. B) UV-vis spectro-electrochemical experiments showing changes during the 1st and 2nd reduction waves of Ru^{II}–≡–Rh^{III} resulting in the formation of Ru^{II}–≡–Rh^{I} (upper panel: difference UV-vis SEC; lower panel: UV-vis SEC); Inset: Cyclic voltammogram of Ru^{II}–≡–Rh^{III} in 0.1 M $TBABF_4$ acetonitrile solution. C) Resonance Raman spectra of Ru^{II}–≡–Rh^{III} (gray) excited at 405 and 643 nm and Ru^{II}–≡–Rh^{I} (green) excited at 643 nm (dissolved in 0.1 M $TBABF_4$ acetonitrile solution, WE: glassy carbon, CE: platinum, RE: Ag/AgCl). The alkyne vibration is highlighted by blue and yellow shading.

Localization of the Franck–Condon region

To localize the Franck-Condon region of the individual absorption events within the binuclear complexes both, in their reduced and non-reduced form, rR spectro-electrochemistry was employed. At 405 nm the Ru-MLCT from the Ru^{II} center to both the bridging ligand and the peripheral tbbpy ligands is excited ($S_{11\text{-}14}$; Table S2).[17] The rR spectrum of Ru^{II}–≡–Rh^{III} collected upon 405 nm excitation shows an alkyne triple bond stretching vibration at 2208 cm^{-1} with moderate intensity (blue shaded area in Figure 1C). The presence of intensive phen-associated rR modes at 1580, 1450 and 1373 cm^{-1} indicates,[8c] that the acceptor orbital of the MLCT transitions is delocalized across the –C≡C– bridge, which is supported by TD-DFT simulations (see charge density difference (CDD) of S_5 in Table S2). This implies an efficient electronic interaction between the Ru(phen) and the Rh(phen) fragment of the complex.[3,17c,18] Upon increasing the excitation wavelength the contribution of $MLCT_{phen}$ states to the rR signatures of Ru^{II}–≡–Rh^{III} increases, but the intensity of the alkyne band is reduced (Figure S2). We interpret this result as a more exclusive localization of the excess electron density on the Ru(phen) moiety of the bridging ligand and hence closer to the Ru photocenter. This is supported by TD-DFT revealing Ru→phen (coordinated to Ru) MLCT states (S_9, 447 nm) at lower energies than Ru→phen (coordinated to Rh, S_{14}, 419 nm; Table S2).

Neither Ru^{II}–≡–Rh^{III} nor Ru^{II}–trz–Rh^{III} absorbs at 643 nm. However, upon Rh^{III}/Rh^{I} reduction, a Rh^{I}-MLCT absorption band appears below 700 nm (Figure 1B).[3] Recording the rR spectrum of Ru^{II}–≡–Rh^{I} at 643 nm, the alkyne vibration is detected at 2174 cm^{-1}, that is, at a similar position as upon 405 nm excitation. This indicates that the acceptor orbital of the Rh^{I}-MLCT (upon excitation at 643 nm) extends to the alkyne group, as it does for the Ru^{II}-MLCT (excited at 405 nm). This is supported by TD-DFT, revealing that the acceptor orbital of both, Ru-MLCT (S_{21}, 470 nm, $f = 0.089$) and Rh-MLCT transitions (S_{19}, 478 nm, $f = 0.049$), are delocalized across the phen–≡–phen bridge (see CDDs in Table S2). In contrast to Ru^{II}–≡–Rh^{I}, the emission of Ru^{II}–trz–Rh^{I} upon excitation at 643 nm is too strong for rR spectra to be recorded reliably (see S3).

Rh^{III}/Rh^{I} reduction of Ru^{II}–≡–Rh^{III} (yielding Ru^{II}–≡–Rh^{I}) shifts the alkyne associated mode by 34 cm^{-1} to lower frequencies, when recording the rR spectrum at 405 nm MLCT (Figure 1C). This red-shift indicates a reduced force constant of the alkyne stretch vibration upon reduction. Thus, we conclude, that the additional charges from the two-electron reduction process

(formally ascribed to the Rh^{III}/Rh^{I} reduction) are partially localized on a π^* orbital of the alkyne triple bond moiety,[3,13b] reducing binding order and force constant. The red-shift of the alkyne stretch vibration is accompanied by an intensity decrease of tbbpy modes at 1185, 1320, 1484 and 1613 cm^{-1}, while the intensity of the phen associated band at 1587 cm^{-1} increases. Jointly, the reduction-induced spectral changes reveal that the acceptor orbital on the alkyne functionality is still accepting electron density upon two electron reduction of the catalytic center (S_5 *vs.* S_{21} in Tables S2 *vs.* S3). This is likely due to structural reorganization of the ligand in response to the Rh^{III}/Rh^{I} reduction, which DFT indicates, showing that the dihedral angle between the two phen-moieties of the phen–≡–phen bridge decreases upon twofold reduction (2 *vs.* 4° in Ru^{II}–≡–Rh^{I} *vs.* Ru^{II}–≡–Rh^{III}).

In contrast, for Ru^{II}–trz–Rh^{III} no spectral changes of the rR spectra recorded upon excitation of the Ru-MLCT (405 nm) are observed upon Rh^{III}/Rh^{I} reduction (yielding Ru^{II}–trz–Rh^{I}, Figure S3): Both Ru^{II}–trz–Rh^{I} and Ru^{II}–trz–Rh^{III} show spectra, which resemble the ones of $[Ru(phen)_3]^{2+}$ complexes.[19] Apparently, the triazole linker suppresses electronic interaction at the Franck-Condon region between the photoexcited Ru(phen) and the Rh(phen) unit. This is supported by DFT calculations, which predict that the phen–trz–phen bridge is not planar but remains rather twisted, with a dihedral angle between the two phen planes of 65° (Ru^{II}–trz–Rh^{III}) and 33° (Ru^{II}–trz–Rh^{I}), respectively.

The rR-SEC studies indicate that the alkyne moiety of Ru^{II}–≡–Rh^{III} takes part as electron accepting unit in both the Ru^{II}-MLCT (Ru^{II}–≡–Rh^{III} and Ru^{II}–≡–Rh^{I}) and the Rh^{I}-MLCT transitions (Ru^{II}–≡–Rh^{I}), which is supported by TD-DFT (see CDDs in Tables S2 and S3). In particular, even upon Rh^{III}/Rh^{I} reduction the Ru^{II}-MLCT transition remains delocalized over the alkyne functionality, thereby indicating that even in the twofold reduced system, vectorial electron transfer from the Ru^{II} photocenter to the catalytically active Rh center might be feasible.

This is notably different to the situation in the functionally related complex $[(tbbpy)_2Ru(tpphz)Rh(Cp^*)Cl]^{3+}$, in which Rh^{III}/Rh^{I} reduction causes the Ru^{II}-MLCT to shift towards the terminal tbbpy ligands.[3] Thus, in terms of vectorial forward electron transfer in the reduced complex upon excitation of the Ru^{II}-MLCT (at *ca.* 400 nm) the bridging ligand in Ru^{II}–≡–Rh^{III} constitutes a promising molecular structure. However, under broad-band excitation Ru^{II}–≡–Rh^{I} will also be exposed to red (600–700 nm) light. In this spectral region a Rh^{I}-MLCT is excited, which discharges the catalytically competent Rh^{I} species and induces back-electron transfer onto the bridging ligand, potentially impeding the light-driven catalytic function of the complex in a not sufficiently acidic environment that prevents protonation of the Rh^{I} center which would switch off this unfavorable process.

Charge transfer dynamics in the reduced complexes

To investigate the charge transfer dynamics in the reduced complexes, we performed femtosecond TA-SEC experiments (Figures 2 and 3) upon excitation i) at 403 nm and ii) at 600 nm, that is, in resonance with MLCT transition of the Ru^{II}(phen) and the Rh^{I}(phen) fragment, respectively.

i) Excitation at 403 nm. Excitation of Ru^{II}–trz–Rh^{I} yields the spectral signatures depicted in Figure 2: a ground-state bleach (GSB) following the steady-state absorption is accompanied by a rather broad, unstructured excited state absorption (ESA) in the red part of the visible spectrum and a comparably sharp ESA band at 355 nm. While the spectral features of Ru^{II}–trz–Rh^{III} do not differ significantly from the data recorded for $[Ru(bpy)_2(phen)]^{2+}$ and $[Ru(phen)_3]^{2+}$chromophores (Figure S4; bpy = 2,2′-bipyridine), electrochemical reduction of the Rh center (Rh^{III}/Rh^{I}) in Ru^{II}–trz–Rh^{I} affects the charge transfer dynamics compared to $[Ru(bpy)_x(phen)_y]^{2+}$-chromophores.[11,15,20] This is evident when looking at the kinetics of the ESA above 500 nm. While the ESA in $[Ru(phen)_3]^{2+}$ complexes is long-lived and does not decay on a time scale of 300 ps,[15,21] the intensity of the ESA is already reduced by more than 50% on this time scale (Figure S4B and E). This finding suggests hole transfer

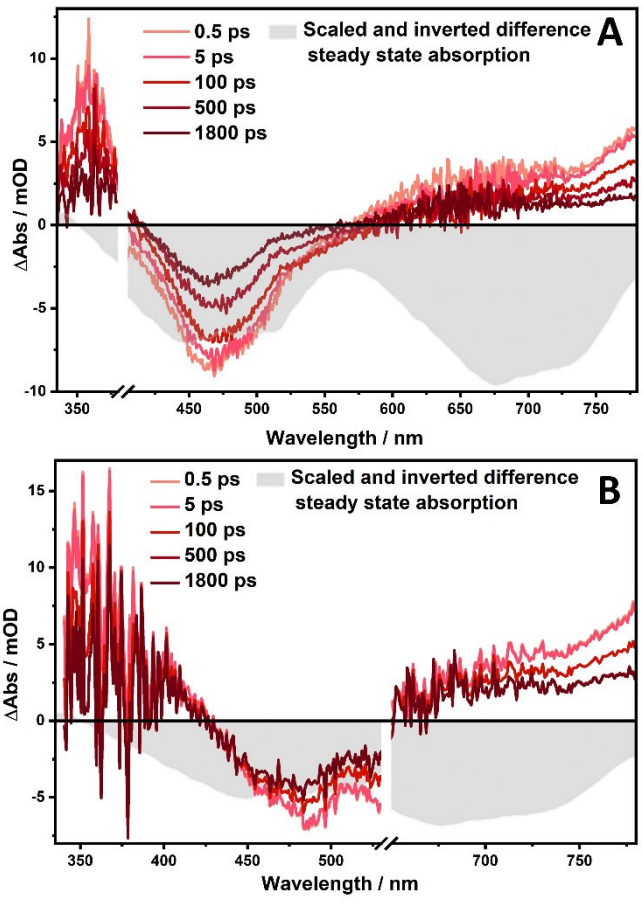

Figure 2. Transient absorption spectra at selected delay times of the electrochemically, twofold-reduced complex Ru^{II}–trz–Rh^{I} upon excitation at A) 403 nm and B) 600 nm in acetonitrile in the presence of 0.1 M $TBABF_4$. The reduced complexes were formed upon applying the corresponding reduction potential for 4 minutes. For comparison, the inverted, that is, negative, difference steady-state absorption spectra of Ru^{II}–trz–Rh^{I} are shown in gray and scaled to the maximum ground-state bleach signal within the individual graphs.

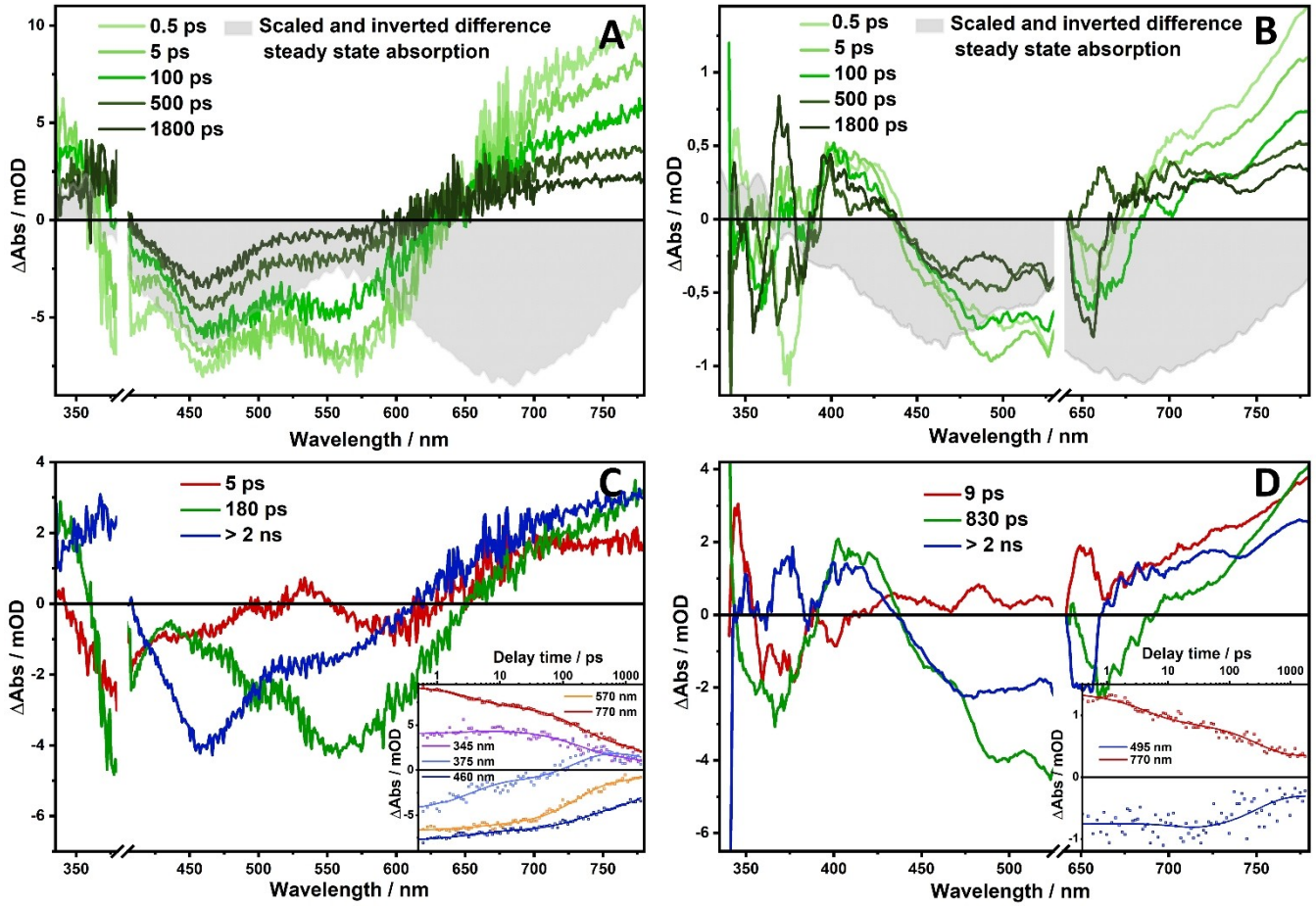

Figure 3. A), B) Transient absorption data including transient absorption spectra at selected delay times and C), D) spectral changes associated with each kinetic process (DAS) of Ru^{II}–≡–Rh^{I} (two-electron reduced) pumped at 403 (A, C) and 600 nm (B, D). Insets in C and D: Transient kinetics at key wavelengths. Spectra recorded after pumping at 600 nm were smoothed due to low signal and signal-to-noise ratio. For comparison, the inverted, that is, negative, differential steady-state absorption spectra of Ru^{II}–≡–Rh^{I} (A, B) are plotted in addition in gray and scaled to the maximum ground-state bleach signal within the individual graphs.

from the photo-oxidized Ru^{III} to the Rh^{I} center (Ru^{III}–$L^{\bullet-}$–Rh^{I}→ Ru^{II}–$L^{\bullet-}$–Rh^{II}, with the characteristic time constant $\tau_2 = 310$ ps). As we do not detect any discernible spectral signature indicative of the Rh^{II}, we conclude that the species resulting from hole transfer, that is, Ru^{II}–$L^{\bullet-}$–Rh^{II} decays rapidly back to the ground state. The remaining molecules, which do not undergo hole transfer cause the long-lived transient absorption signature. In particular, the system does not allow for electron transfer from the photoexcited Ru(phen) unit towards the Rh^{I} center. This is supported by calculations of orbital energy levels of selected molecular orbitals of Ru^{II}–trz–Rh^{I} which show that the triazole is a charge transfer barrier for electrons but not electron holes (Figure S6).

In contrast, excitation of the Ru^{II} center in the reduced complex Ru^{II}–≡–Rh^{I} (Figure 3A) leads to TA spectra significantly different from the non-reduced complex Ru^{II}–≡–Rh^{III}.[11] Following excitation of the Ru^{II}-MLCT, a strong excited state absorption feature above 620 nm and negative differential absorption features at 460 and 565 nm appear immediately (Figure 3A and C). While the negative band at 460 nm corresponds to ground-state bleach of the Ru^{II}-MLCT transitions we associate the negative band at 565 nm with the bleach of the Rh^{I}-MLCT transitions in Ru^{II}–≡–Rh^{I}, because the bleach spectrally overlaps with the Rh^{I}-MLCT absorption band (Figure 1B, upper panel, and Figure S5); this is further in agreement with TD-DFT calculations (S_6, 650 nm). As excitation at 403 nm does not address the latter transitions directly, we conclude that rapid hole transfer Ru^{III}–$L^{\bullet-}$–Rh^{I}→Ru^{II}–$L^{\bullet-}$–Rh^{II} appears within the temporal resolution of our experimental setup (*i.e.*, 300 fs; Scheme 2). This ultrafast hole transfer is followed by cooling and energy dissipation ($\tau_1 = 5$ ps). Subsequently, the electron density residing on the bridge relaxes towards the Rh^{II} center, regaining the original Ru^{II}–L–Rh^{I} species ($\tau_2 = 180$ ps). The DAS(τ_2) thus reflects the decay of the reduced alkyne absorption at around 350 nm,[11,22] while the negative band at 375 nm reflects the decay of $MLCT_{bpy}$ GSB contributions.[15] The latter transitions are bleached as initial excitation partially populates tbbpy-associated Ru^{II}-MLCT states (e.g., S_{21}; Table S2), which also relax towards the Rh center during the process experimentally associated with τ_2.

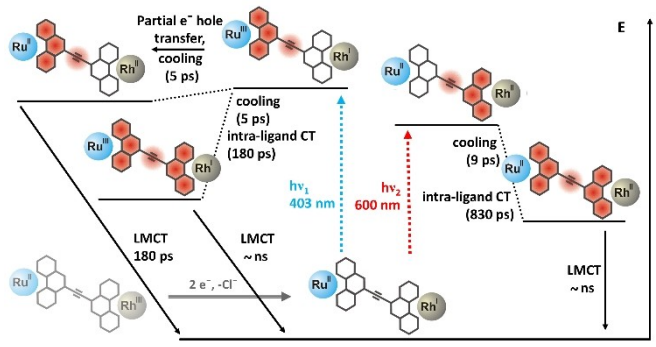

Scheme 2. Schematic representation of the two proposed photophysical pathways for the catalytically active photocatalyst Ru^{II}–≡–Rh^{I}. The twofold-reduced species Ru^{II}–≡–Rh^{I} is generated by electrochemical reduction of Ru^{II}–≡–Rh^{III} (bottom left, gray shaded). Subsequently the reduced species Ru^{II}–≡–Rh^{I} is optically excited either at around 400 or at 600 nm (TA data at 403 and 600 nm; rR data at 405 and 643 nm). At 403 nm an MLCT from Ru^{II} to the adjacent phen moiety and the alkyne functionality of the bridging ligand is excited. In one ensemble of molecules, an electron hole is then partially transferred on a sub-500 fs timescale, reducing Ru^{III} (to Ru^{II}) and oxidizing the Rh^{I} center (to Rh^{II}), followed by a ligand-to-metal charge transfer (LMCT) towards the Rh^{II}, finally regaining the ground-state species Ru^{II}–≡–Rh^{I} within 180 ps. Another ensemble of molecules decays upon 403 nm excitation via a relaxation channel including an intraligand CT which results in a state with excess electron density partially localized on both of the phen parts. This state decays through a LMCT of ns lifetime to the ground-state Ru^{II}–≡–Rh^{I}. In contrast, at 600 nm excitation, an MLCT from Rh^{I} to the phen fragment is excited, which decays via an intraligand CT and an LMCT to the ground state, i.e., Ru^{II}–≡–Rh^{I}. The catalytically active Rh^{I} is maintained in the second path of longest lifetime.

We tentatively relate the observation of a long-lived component ($\tau_3 > 2$ ns) to non-quantitative electron transfer to the Rh center and the presence of an intraligand charge-transfer state, in which the charge density is not localized in an antibonding orbital of the alkyne moiety but, due to a reduction induced distortion of the central structural motif, partially localized on either of the phen-moieties, Ru^{III}–δ^-–≡–δ^-–Rh^{I} or Ru^{II}–δ^-–≡–δ^-–Rh^{II} (Scheme 2). Hence, the differential absorption spectrum associated with this intraligand charge-transfer conformation reflects partial bleach of the Ru^{II}-MLCT and the Rh^{I}-MLCT transitions, albeit the latter one drastically reduced.

ii) Excitation at 600 nm. Upon excitation of the Rh^{I}-MLCT at 600 nm the choice of the bridging ligand, that is, –≡– versus –trz–, significantly impacts the photoinduced dynamics in the Ru-BL–Rh complexes. Considering Ru^{II}–trz–Rh^{I}, the TA signatures upon 600 nm excitation differ only slightly in the structure of the ESA above 670 nm in comparison to the TA spectra recorded upon 403 nm excitation (Figure 2A).[11] We rationalize this result considering that the excited-state properties are determined by the reduced phen moiety, which acts as charge accepting moiety in both the Ru^{II}-MLCT and Rh^{I}-MLCT transitions. As the triazole linker effectively interrupts electronic interactions between the two metal centers, the Rh^{I}-MLCT excitation remains localized in the Rh sphere (S_6, 651 nm; Table S4), and features comparably strong ESA associated with the reduced phen moiety. Thus, the overall features of the TA spectra do not depend significantly on the metal center itself, comparing Ru^{II}-MLCT versus Rh^{I}-MLCT excitation. However, a red-shift of 10 nm of the GSB feature is observed comparing 403 to 600 nm excitation.

Considering the photoinduced processes in Ru^{II}–≡–Rh^{I} upon excitation of the Rh^{I}-MLCT at 600 nm, TA spectra are observed, which are depicted in Figure 3B. The initial TA spectrum (recorded at a delay time of 300 fs) reveals a GSB centered at 490 nm, accompanied by ESA centered between 395 and 430 nm and longer than 690 nm. While the overall shape of the TA signal is similar to the spectra observed upon 403 nm excitation, the pronounced double-minimum GSB is absent upon 600 nm excitation and the excited state relaxation kinetics are altered. The first kinetic process, which is associated with a characteristic time constant of 9 ps, reflects a decay of the long-wavelength absorbance and a slight red-shift of the ΔOD zero crossing point from about 665 to 690 nm. While these spectral shifts are observed, the ΔOD signals in the region of the GSB only marginally change. We ascribe this process to structural relaxation of the photoinduced complex and excess-energy dissipation to the solvent.

The second kinetic component, identified by multi-exponential fitting, $\tau_2 = 830$ ps, spectrally resembles the 180 ps component observed for Ru^{II}–≡–Rh^{I} upon 403 nm excitation Negative differential absorption features at 370, 490 nm and in the vicinity of the pump wavelength, that is, at about 600 nm, are accompanied by an ESA band at a probe wavelength longer than 685 nm. In addition, a positive ΔOD band is observed at around 410 nm. In the respective spectral position, a local maximum (however with an overall negative ΔOD) was observed upon 403 nm excitation. Based on these spectral features and the similarities to the data obtained upon 403 nm excitation, we associated the 830 ps component with the decay of the Ru^{II}–$L^{\bullet-}$–Rh^{II} species, which directly results from the excitation of the Rh^{I}-MLCT transition at 600 nm (Scheme 2). Also, under these excitation conditions, a long-lived component ($\tau_3 > 2$ ns) is observed. The key spectral characteristics of this component are an ESA at wavelength longer than 660 nm and a comparably broad negative ΔOD band extending from 435 to 660 nm. This band indicates two separate, equally intense minima, one at about 475 nm and the second one in the vicinity of the pump wavelength (Figure 3D). This is reminiscent of the shape of the long-lived differential absorption spectrum obtained upon 403 nm excitation.

Hence, we ascribe the signatures to a twisted intramolecular charge-transfer state. As pump pulses centered at 600 nm exclusively excited the Rh^{I}-MLCT state, we assign the electronic configuration of this intramolecular charge-transfer state exclusively to Ru^{II}–δ^-–≡–δ^-–Rh^{II}, excluding Ru^{III}–δ^-–≡–δ^-–Rh^{I} as a possible option.

Conclusion

Comparing the photoinduced electron-transfer kinetics in the catalytically active intermediates of two catalysts for light-driven NAD^+ reduction, Ru^{II}–≡–Rh^{I} and Ru^{II}–trz–Rh^{I}, poses the challenge of experimentally accessing the generally short-lived,

highly reactive intermediates in a sub-ps time-resolved transient absorption experiment. We addressed this problem by applying transient absorption spectro-electrochemistry, that is, electrochemically reducing the catalysts to the respective Rh^{I} species followed by spectroscopic characterization. We show that utilizing the –trz– bridge between the Ru^{II} photocenter and the Rh^{I}(Cp*) catalytic center raises the orbitals on the bridge to such an extent that light-activated electron transfer across the bridge, from the Ru to the Rh center, is impeded, irrespective of whether the Ru^{II}-MLCT transition (at 405 nm) or the Rh^{I}-MLCT transition (at 643 nm) is excited. In contrast, the –≡– bridge facilitates electronic interaction between both metal centers upon excitation of either of the MLCT transitions. The facile electron transfer across the –≡– bridge might be one reason for the high initial activity of the catalyst. In particular, the identification of two possible decay channels upon Ru^{II}-MLCT excitation in Ru^{II}–≡–Rh^{I} demonstrates the positive impacts of the alkyne linker. Excitation leads either to a short-lived (compared to the analogous tpphz-based system[3]) Ru^{II}–$L^{\bullet-}$–Rh^{II} intermediate featuring a discharged catalytic center for only about 150 ps or to a rather long-lived Ru^{III}–$L^{\bullet-}$–Rh^{I} species, capable of additional electron extraction from sacrificial donors under photocatalytic conditions, which would lead to a threefold-reduced complex. However, our data show that, upon photoexcitation of Ru^{II}–≡–Rh^{I}, increased electron density remains on the alkynyl functionality of the symmetric bridging ligand. This, in turn, favors reduction of the triple bond, which is considered the prime deactivation channel of the catalyst under operando conditions. Thus, desymmetrization of the bridging ligand, for example, by introducing a Rh-coordinating phenanthroline moiety with significantly lowered π^* energy, might localize the excess electron density onto the Rh side of the ligand and hence off the alkynyl moiety (Scheme 2). Although this might reduce the deactivation of the catalyst, it might also prevent "discharging" of the activated catalyst as a result of excited-state electron transfer following excitation of the Rh^{I}-MLCT.

This is observed for the alkyne linker in this work. In comparison to the tpphz bridging ligand, the alkyne bridge enables faster directional charge transfer from the photocenter even to the reduced catalytic center, but illumination with red light initiates the reverse charge-transfer process from the reduced Rh center towards Ru, which limits the lifetime of the charge-separated state and therefore the catalytic efficiency.[11] The triazole linker, on the other hand, slows down the charge transfer from the photocenter to the catalytic center, but stabilizes the charge-separated state and blocks the charge transfer back to the Ru center upon excitation at 600 nm. This results in a long-lived, charge-separated state, and explains the similar catalytic activity of Ru^{II}–≡–Rh^{III} and Ru^{II}–trz–Rh^{III}.[11] Finally, the sequence of electrochemical two-electron reduction followed by Ru-MLCT excitation triggering hole transfer from the Ru to the Rh center, paves the way towards understanding the electron-transfer kinetics of a twofold-reduced Ru–BL–Rh complex. Such a twofold-reduced Ru–BL–Rh complex would – under catalytic conditions – result from reductive quenching of the photoexcited complex. Correlating the electrochemical potentials of the linker structure in the different bridging ligands, forward electron transfer yielding Ru^{II}–BL–Rh^{I} is faster for the –trz– system compared to the –≡– linker.

Experimental Section

Ru^{II}–≡–Rh^{III} and Ru^{II}–trz–Rh^{III} were synthesized as described previously.[11] Solutions in anhydrous acetonitrile (Sigma-Aldrich) containing 0.1 M tetrabutylammonium hexafluoroborate ($TBABF_4$) yielding an optical density of 0.3 at 400 nm in a 1 mm cuvette were degassed with argon prior to spectroscopic and electrochemical measurements performed at room temperature. UV-vis–spectro-electrochemistry (SEC), resonance Raman (rR) SEC and electrochemical measurements were performed using a thin-layer spectro-electrochemical cell (Hellma, Bioanalytical Systems, USA) of 1 mm pathlength employing Pt counter electrode, Ag/AgCl pseudo-reference electrode and glassy carbon working electrode controlled by a VersaSTAT 3 (Princeton Applied Research) potentiostat for cyclic voltammetry (CV) and measurements at fixed potential. UV-vis spectra were recorded in transmission mode with a single-channel fiber-optic spectrometer (AvaSpec-ULS2048XL) and a deuteriumhalogen light source (AvaLight DH–S-BAL).

RR measurements were performed with 5 mW laser power upon excitation at 405 and 643 nm. The Raman scattered light was detected by an IsoPlane 160 spectrometer equipped with a thermoelectrically cooled CCD camera (Princeton Instruments, USA) with 50 μm slit width of and 600 or 1200 grooves/mm diffraction gratings. The acetonitrile band at 1373 cm^{-1} was used for normalization and wavenumber calibration.

Transient absorption spectroscopy was performed using a custom build setup as described in detail elsewhere.[21] Briefly, 403, 492 or 600 nm pump pulses of approximately 100 fs pulse duration at 500 Hz repetition rate and a white-light supercontinuum probe pulse at 1 kHz repetition rate are focused onto the sample to analyze the excited state dynamics with 300 fs temporal resolution.[23] The mutual polarization between pump and probe pulses was set to magic angle.

The sample is dissolved in anhydrous acetonitrile and contained in a cell with 1 mm path length ($OD_{400\ nm} = 0.3$) equipped with a custom 0.4 mm thick glassy carbon working electrode allowing pump and probe beam to pass collinearly through a 1-mm hole in the glassy carbon electrode. This arrangement ensures high yields of the redox-active species within the observation volume.

Customized electronics and control software (Pascher Instruments AB, Sweden) allow for simultaneously measuring steady-state absorption, cyclic voltammetry (CV), chronoamperometry and TA and ensure jitter-free timing of the datasets. The spectra of the probe and of reference pulses, generated from the same supercontinuum's pulse, are detected by a diode array detector (Pascher Instruments AB, Sweden) mounted on a 150 mm focal length Czerny–Turner spectrograph (SP2150, Princeton Instruments).

The transient absorption data was pre-processed (chirp and background correction) and globally analyzed using the KiMoPack python package.[24] The data were fitted with a parallel decay model (yielding decay associated spectra). The respective errors of the fitted rate constants ($> 0.0005\ ps^{-1}$) were determined in a confidence interval of 95 % (Table S1).

Both TA and steady-state UV-vis spectra of the electrochemically reduced complexes were simultaneously recorded at a set of potentials (after the current has reached its respective plateau value). Simultaneously recording UV-vis absorption and TA spectra

enables us to assess the concentration of the redox active species within the observation volume, the conversion efficiency of the electrochemical process and to monitor sample integrity and additional product formation during the measurement. Comprehensive experimental details and methods can be found in the Supporting Information.

Acknowledgements

Supported by the Deutsche Forschungsgemeinschaft (DFG, German Research Foundation) – Projektnummer 364549901 – TRR 234 [A1, A4, Z2]. P. W. thankfully acknowledges financial support by the Studienstiftung des deutschen Volkes. C. M. thankfully acknowledges financial support from the Fonds der Chemischen Industrie by a Kekulé Stipendium. Open Access funding enabled and organized by Projekt DEAL.

Conflict of Interest

The authors declare no conflict of interest.

Data Availability Statement

The data that support the findings of this study are available from the corresponding author upon reasonable request.

Keywords: photocatalysis · resonance Raman spectroscopy · spectro-electrochemistry · transient absorption · ultrafast spectroscopy

[1] a) G. F. Manbeck, K. J. Brewer, *Coord. Chem. Rev.* **2013**, *257*, 1660–1675; b) T. R. Cook, D. K. Dogutan, S. Y. Reece, Y. Surendranath, T. S. Teets, D. G. Nocera, *Chem. Rev.* **2010**, *110*, 6474–6502; c) H. Ozawa, K. Sakai, *Chem. Commun.* **2011**, *47*, 2227–2242; d) S. M. Arachchige, J. R. Brown, E. Chang, A. Jain, D. F. Zigler, K. Rangan, K. J. Brewer, *Inorg. Chem.* **2009**, *48*, 1989–2000.

[2] M. Schulz, N. Hagmeyer, F. Wehmeyer, G. Lowe, M. Rosenkranz, B. Seidler, A. Popov, C. Streb, J. G. Vos, B. Dietzek, *J. Am. Chem. Soc.* **2020**, *142*, 15722–15728.

[3] L. Zedler, A. K. Mengele, K. M. Ziems, Y. Zhang, M. Wächtler, S. Gräfe, T. Pascher, S. Rau, S. Kupfer, B. Dietzek, *Angew. Chem. Int. Ed.* **2019**, *58*, 13140–13148; *Angew. Chem.* **2019**, *131*, 13274–13282.

[4] a) A. J. Esswein, D. G. Nocera, *Chem. Rev.* **2007**, *107*, 4022–4047; b) S. Bold, T. Straistari, A. B. Muñoz-García, M. Pavone, V. Artero, M. Chavarot-Kerlidou, B. Dietzek, *Catalysts* **2020**, *10*, 1340.

[5] a) J.-F. Lefebvre, J. Schindler, P. Traber, Y. Zhang, S. Kupfer, S. Gräfe, I. Baussanne, M. Demeunynck, J.-M. Mouesca, S. Gambarelli, V. Artero, B. Dietzek, M. Chavarot-Kerlidou, *Chem. Sci.* **2018**, *9*, 4152–4159; b) R. Konduri, N. R. de Tacconi, K. Rajeshwar, F. M. MacDonnell, *J. Am. Chem. Soc.* **2004**, *126*, 11621–11629.

[6] Q. Pan, L. Freitag, T. Kowacs, J. C. Falgenhauer, J. P. Korterik, D. Schlettwein, W. R. Browne, M. T. Pryce, S. Rau, L. González, J. G. Vos, A. Huijser, *Chem. Commun.* **2016**, *52*, 9371–9374.

[7] S. Tschierlei, M. Presselt, C. Kuhnt, A. Yartsev, T. Pascher, V. Sundstrom, M. Karnahl, M. Schwalbe, B. Schafer, S. Rau, M. Schmitt, B. Dietzek, J. Popp, *Chemistry* **2009**, *15*, 7678–7688.

[8] a) S. Bold, L. Zedler, Y. Zhang, J. Massin, V. Artero, M. Chavarot-Kerlidou, B. Dietzek, *Chem. Commun.* **2018**, *54*, 10594–10597; b) S. Mendes Marinho, M.-H. Ha-Thi, V.-T. Pham, A. Quaranta, T. Pino, C. Lefumeux, T. Chamaillé, W. Leibl, A. Aukauloo, *Angew. Chem. Int. Ed.* **2017**, *56*, 15936–15940; *Angew. Chem.* **2017**, *129*, 16152–16156; c) Y. Zhang, P. Traber, L. Zedler, S. Kupfer, S. Grafe, M. Schulz, W. Frey, M. Karnahl, B. Dietzek, *Phys. Chem. Chem. Phys.* **2018**, *20*, 24843–24857; d) S. Goia, M. A. P. Turner, J. M. Woolley, M. D. Horbury, A. J. Borrill, J. J. Tully, S. J. Cobb, M. Staniforth, N. D. M. Hine, A. Burriss, J. V. Macpherson, B. R. Robinson, V. G. Stavros, *Chem. Sci.* **2022**, *13*, 486–496.

[9] a) S. Bold, J. Massin, E. Giannoudis, M. Koepf, V. Artero, B. Dietzek, M. Chavarot-Kerlidou, *ACS Catal.* **2021**, *11*, 3662–3678; b) K. L. Materna, A. M. Beiler, A. Thapper, S. Ott, H. Tian, L. Hammarström, *ACS Appl. Mater. Interfaces* **2020**, *12*, 31372–31381; c) M. S. Eberhart, L. M. R. Bowers, B. Shan, L. Troian-Gautier, M. K. Brennaman, J. M. Papanikolas, T. J. Meyer, *J. Am. Chem. Soc.* **2018**, *140*, 9823–9826; d) Y. Farré, F. Maschietto, J. Föhlinger, M. Wykes, A. Planchat, Y. Pellegrin, E. Blart, I. Ciofini, L. Hammarström, F. Odobel, *ChemSusChem* **2020**, *13*, 1844–1855.

[10] P. Gotico, T.-T. Tran, A. Baron, B. Vauzeilles, C. Lefumeux, M.-H. Ha-Thi, T. Pino, Z. Halime, A. Quaranta, W. Leibl, A. Aukauloo, *ChemPhotoChem* **2021**, *5*, 654–664.

[11] L. Zedler, P. Wintergerst, A. K. Mengele, C. Müller, C. Li, B. Dietzek-Ivansic, S. Rau, *Nature Communications* **2022**, *13*, 2538.

[12] S. Chardon-Noblat, S. Cosnier, A. Deronzier, N. Vlachopoulos, *J. Electroanal. Chem.* **1993**, *352*, 213–228.

[13] a) A. K. Mengele, S. Kaufhold, C. Streb, S. Rau, *Dalton Trans.* **2016**, *45*, 6612–6618; b) M. Ladwig, W. Kaim, *J. Organomet. Chem.* **1991**, *419*, 233–243.

[14] R. M. Berger, J. R. Holcombe, *Inorg. Chim. Acta* **1995**, *232*, 217–221.

[15] C. W. Stark, W. J. Schreier, J. Lucon, E. Edwards, T. Douglas, B. Kohler, *J. Phys. Chem. A* **2015**, *119*, 4813–4824.

[16] F. Lux, G. Lemercier, C. Andraud, G. Schull, F. Charra, *Mol. Cryst. Liq. Cryst.* **2008**, *485*, 881–886.

[17] a) L. Zedler, J. Guthmuller, I. R. de Moraes, S. Kupfer, S. Krieck, M. Schmitt, J. Popp, S. Rau, B. Dietzek, *Chem. Commun.* **2014**, *50*, 5227–5229; b) L. Zedler, S. Kupfer, I. R. de Moraes, M. Wachtler, R. Beckert, M. Schmitt, J. Popp, S. Rau, B. Dietzek, *Chem. Eur. J.* **2014**, *20*, 3793–3799; c) M. Wachtler, J. Guthmuller, L. Gonzalez, B. Dietzek, *Coord. Chem. Rev.* **2012**, *256*, 1479–1508.

[18] S. Tschierlei, M. Karnahl, M. Presselt, B. Dietzek, J. Guthmuller, L. González, M. Schmitt, S. Rau, J. Popp, *Angew. Chem. Int. Ed.* **2010**, *49*, 3981–3984; *Angew. Chem.* **2010**, *122*, 4073–4076.

[19] a) W. Chen, C. Turro, L. A. Friedman, J. K. Barton, N. J. Turro, *J. Phys. Chem. B* **1997**, *101*, 6995–7000; b) W. R. Browne, J. J. McGarvey, *Coord. Chem. Rev.* **2006**, *250*, 1696–1709.

[20] a) Y. Sun, Y. Liu, C. Turro, *J. Am. Chem. Soc.* **2010**, *132*, 5594–5595; b) N. Yoshikawa, S. Yamabe, S. Sakaki, N. Kanehisa, T. Inoue, H. Takashima, *J. Mol. Struct.* **2015**, *1094*, 98–108.

[21] R. Siebert, D. Akimov, M. Schmitt, A. Winter, U. S. Schubert, B. Dietzek, J. Popp, *ChemPhysChem* **2009**, *10*, 910–919.

[22] P. Wintergerst, A. K. Mengele, D. Nauroozi, S. Tschierlei, S. Rau, *Eur. J. Inorg. Chem.* **2019**, *14*, 1988–1992.

[23] A. L. Dobryakov, S. A. Kovalenko, N. P. Ernsting, *J. Chem. Phys.* **2005**, *123*, 044502.

[24] J. Uhlig, C. Müller, T. Pascher, A. Eriksson, *KiMoPack* **2022**, https://doi.org/10.5281/zenodo.5720587.

Manuscript received: February 15, 2022
Accepted manuscript online: April 28, 2022
Version of record online: May 23, 2022